Int J Adv Manuf Technol (2017) 89:463–473
DOI 10.1007/s00170-016-9107-1

ORIGINAL ARTICLE

High-performance grinding of a 2-m scale silicon carbide mirror blank for the space-based telescope

Zhiyu Zhang[1] · **Xu Yang**[2] · **Ligong Zheng**[1] · **Donglin Xue**[1]

Received: 21 February 2016 / Accepted: 26 June 2016 / Published online: 5 July 2016

Abstract Silicon carbide (SiC) is a competitive candidate material for building the space-based reflecting mirrors. However, SiC is also a typical difficult-to-machine material due to its extreme hardness. When SiC workpiece is machined by grinding, the wheel wears rapidly which leads to a deterioration of surface form accuracy. Grinding efficiency also becomes extremely low due to the frequent truing and dressing of grinding wheels. To achieve high-performance grinding process capable of producing accurate surface at high grinding efficiency, an ultrasonic vibration-assisted fix-point grinding technology was developed in this study. Wheel wear observation indicated that the wheel needs not to be dressed during the whole grinding cycle. Moreover, a laser tracker was used to achieve an on-machine measurement of the surface form error. A CNC tool microset was adopted to evaluate the wheel wear amount. On the basis of the above two results, surface form error could be predicted before grinding, and thus, an in-process compensation of surface form error was carried out. Using the above-mentioned grinding strategies, a SiC mirror blank with an aperture diameter of 2 m was successfully ground to a form accuracy of 18 μm in peak-to-valley (PV). Therefore, this work provides an efficient and economical solution for grinding the large-scale SiC aspherical surfaces.

Keywords High-performance grinding · Wheel wear compensation · Five-axis machining · Tool path generation · Reaction-bonded SiC

✉ Zhiyu Zhang
zhangzhiyu@ciomp.ac.cn

[1] Changchun Institute of Optics Fine Mechanics and Physics, Chinese Academy of Sciences, Changchun, China

[2] Jilin University, Changchun, China

1 Introduction

Hubble space telescope (HST) is a best-known space-based telescope that is placed in orbit around the Earth. The optics of the HST include a 2.4-m diameter primary mirror made of ultra low expansion (ULE) glass and a 0.3-m secondary mirror made of Zerodur glass [1–4]. It has been long suggested that silicon carbide (SiC) would be a competitor material to ULE and Zerodur for building the next-generation large-scale reflecting mirrors, particularly used in the space-based telescope, owing to its high stiffness-to-density ratio and low thermal distortion properties [5–7]. However, SiC is a typical difficult-to-machine material because of its extreme hardness, only lower than diamond, cubic boron nitride (cBN), and boron carbide (B_4C) [8]. The extreme hardness induced an extremely low material removal rate. For example, Zygo Corporation has reported that even using diamond abrasive, the material removal rate of SiC is approximately 1/35th that of fused silica and less than 1/50th that of Zerodur.

On the other hand, the advantages of aspherical elements over spherical ones are well recognized for its reduced weight, improved performance, and lower cost. Present "state of the art" manufacturing procedures for SiC aspherical mirrors are started from successive grinding, followed by computer-controlled subaperture lapping and polishing processes. Afterward, high-deterministic processes such as magnetorheological finishing and ion beam figuring are always used to achieve necessary form accuracy typically less than 100 nm in peak-to-valley (PV) [9–11]. The grinding is a high efficiency process, and its material removal rate is about 20~50 times of that of the subsequent processes. Therefore, it is highly expected that form accuracy of the ground surface could be as close as the targeted values, thus greatly reducing the subsequent production cycles.

As for grinding of a small SiC spherical surface with an aperture of 13.5 mm, submicron form accuracy could be

directly achieved by utilizing an ultra-precision machine tool and well-dressed metal-bond grinding wheels [12]. However, the form accuracy deteriorates rapidly when grinding a large-scale workpiece, mainly due to severe wheel wear. For example, Cranfield University in 2005 had developed a three-axis ultra-precision grinding machine, called BoX®, and reported their research on grinding of a hexagonal SiC part with 400 mm across corners [13, 14]. Experimental results showed that severe wheel wear occurred and the diamond wheel required to be dressed each 26.5 min to maintain a normal grinding force. The final achieved form accuracy of the 400-mm scale SiC workpiece was only 5 μm in PV, significantly larger than the results reported in reference 12. It can thus be known that precisely and efficiently grinding of large-scale SiC is a challenge task.

To the best of our knowledge, until now, there exists little information reported on the machining technologies and the obtainable form accuracy for even larger SiC component. In this work, a five-axis fix-point grinding mode was developed for rapidly and accurately machining a 2-m scale aspherical SiC mirror blank. Rotary ultrasonic grinding system was adopted to realize a non-dressing grinding process, which means that the wheel needs not to be dressed during the whole grinding cycle. A commercial laser tracker was used to achieve an on-machine measurement of the surface form error. A CNC tool microset was also used to evaluate the wheel wear amount. On the basis of the above two results, wheel wear amount could be predicted before grinding, and thus, an in-process compensation of surface form error was developed. Subsurface damages of the ground SiC surface were also investigated by SEM observation and EDX analysis. It is expected that the present study could provide a very efficient and economical method for high-performance grinding of large-scale SiC aspherical surfaces.

2 Experimental details

2.1 Workpiece

Conventional methods for manufacturing SiC ceramic material include pressureless sintering, gas pressure sintering, hot pressing, and reaction-bonding (RB) technology. The RB-SiC was fabricated by infiltrating silicon (Si) melt into a green compact consisting of C and SiC powders (α-SiC). The liquid Si reacts with the C particles, forming new SiC particles (β-SiC). However, the infiltrated Si cannot react with C completely, and any excess Si fills remaining large pores in the body as well as boundary space among SiC grains. Thus, dense SiC-Si composite with excessive silicon as bonding material is produced [16]. By several decades' effort, we have successfully developed a gelcasting process for sintering large-scale optical grade RB-SiC mirror blanks [15]. In this study, a RB-SiC mirror blank in aperture diameter of 2000 mm was fabricated. Different from a monolithic mirror, the 2000-mm mirror blank was welded together by six fan-shaped segments as shown in Fig. 1a. The joined grinding workpiece as shown in Fig. 1b has rough casting spherical surface in radius of about 7000 mm. The designed mirror surface is a convex paraboloid having equation of $y^2 = 12000x$. Initial form error of workpiece surface before grinding was 4000 μm in PV, which was measured by using an on-machine profilometer probe.

2.2 Five-axis fix-point grinding mode

As shown in Fig. 2a, a three-axis arc-enveloped grinding mode is conventionally used for grinding aspherical surfaces with rotational symmetry [17]. In this mode, the grinding point is variable on the arc-shaped wheel surface because the axial direction of the grinding wheel remains constant. This mode can average wheel wear and prolong wheel life when grinding large workpieces. However, both complicated calculation of shifting contact point and high-accuracy truing of wheel to keep its accurate profile are required, which severely reduce grinding efficiency.

In order to increase grinding efficiency, a four-axis fix-point grinding mode as shown in Fig. 2b was proposed [18]. In this mode, the grinding point remains constant during grinding as a result of the *B*-axis rotation. This grinding mode eliminates contact point calculation and has a very low

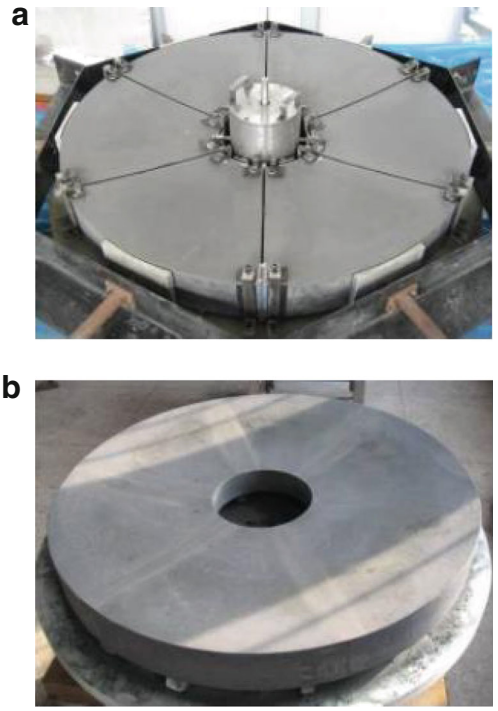

Fig. 1 Photos of reaction-bonded SiC workpiece: **a** before welding and **b** after welding

requirement of wheel profile accuracy. A remarkable problem is that wheel wears rapidly at the fixed grinding point, which will introduce a gradually increased form error on ground surface. Fortunately, this low-frequency error could be significantly reduced by a proper compensation grinding.

To achieve fix-point grinding of aspherical surface without rotational symmetry (such as off-axis aspherical surface) as shown in Fig. 2c, an additional *Y*-axis motion is also needed to adjust the wheel-axis angle according to the random variation of surface normal vector. In this study, a five-axis (XYZBC) fix-point grinding mode is developed for grinding large-scale complicated SiC mirror blanks including the off-axis aspherical surfaces.

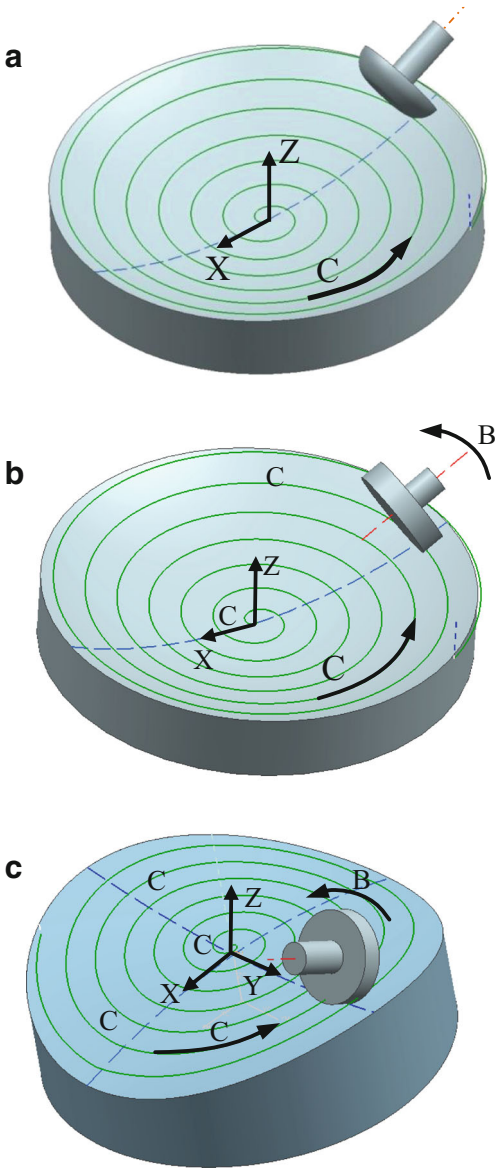

Fig. 2 The schematics of **a** three-axis arc-enveloped grinding mode, **b** four-axis fix-point grinding mode, and **c** five-axis fix-point grinding mode

2.3 Grinding machining center

Grinding experiments were carried out on a five-axis (XYZBC) numerically controlled machining center (ULTRASONIC 210-P SAUER, DMG Corporation, Germany). Figure 3 shows the mounting of workpiece onto the machining center. Figure 4 shows the workpiece on the turntable of the machining center. The configuration of the machining center is shown in Fig. 5. The traverse ranges of *X*-, *Y*-, and *Z*-axes are 2100, 1800, and 762 mm, respectively. The repetitive positioning accuracy of the linear axes is 8 μm in whole traverse range. It needs to point out that the *B*-axis head of the machining center is different from a standard orthogonal machining center configuration. The *B*-axis head has a swivel range of −10°~+120°. It is originally designed for realizing both vertical and horizontal machining in a single machine. Such a configuration makes it ideally suited for machining curved surfaces.

2.4 Ultrasonic vibration system

As shown in Fig. 6, ultrasonic vibration system was adopted on this five-axis machining center, which enables rotary ultrasonic machining by vibrating the wheel along wheel-axis direction at ultrasonic frequency. Figure 7 is a schematic diagram of the inclined axis rotary ultrasonic machining, in which the wheel is ultrasonically vibrated along the wheel axis during grinding. The ultrasonic vibration is generated by the ultrasonic wave generator and transmitted to the piezoelectric device inside of the special tool by the electric inductor attached to the end face of the spindle.

2.5 Grinding conditions

Cup-like resin-bonded diamond wheels were used in grinding. Each grinding wheel has a 100-mm outer diameter and a 10-mm thickness. The width of abrasive layer is 5 mm with grit size of 126 μm. No truing and no dressing of grinding wheel were performed before and during grinding. That is because known

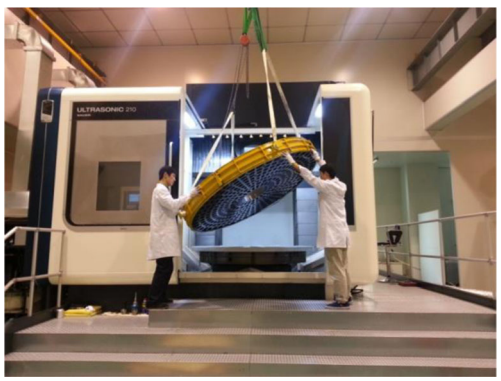

Fig. 3 Mounting of the 2-m workpiece onto the machining center

Fig. 4 2-m SiC mirror blank under grinding

from our former research that the SiC grains on workpiece surface functioned as a dressing tool slowly scratching the resin matrix of the diamond wheel during grinding process [19].

Before grinding the 2-m workpiece, several miniature SiC samples were used to optimize the grinding conditions. After that, the grinding of the 2-m workpiece was carried out. The conditions of the grinding experiment are listed in Table 1. Ultrasonic vibration frequency was automatically set in the operation system of machine center by sensing the largest amplitude of the wheel vibration.

3 Results

3.1 Wheel wear observation

When a grinding wheel is subject to wear during long-term grinding process, the abrasive layer as well as the diamond grits wears out. Figure 8a shows the image of the unused wheel. Figure 8b, c shows the worn wheel after the first and the second grinding cycle, respectively. It can be seen that the abrasive layer is significantly worn out. To investigate the diamond grits, the unused wheel surface and the worn surface are, respectively, examined using the scanning electron microscope (SEM). Comparing Fig. 9b with Fig. 9a, no detectable difference could be found on the diamond grits between the unused wheel surface and the worn one. That is to say, the diamond grits are sharp enough for use again. Therefore, no dressing work is needed in the whole grinding cycles. That is obviously different from the wheel wear phenomenon which shows only worn of the diamond grits. The observation results also indicate that the thickness of abrasive layer dominates the grinding wheel working life. In addition, some grinding debris can be seen on the worn surface. Diamond grit pullout is also clearly found in Fig. 9b.

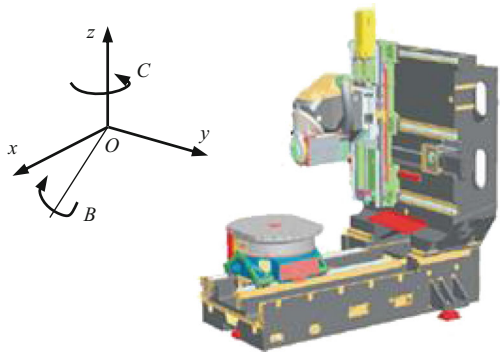

Fig. 5 Axis configuration of the used machining center

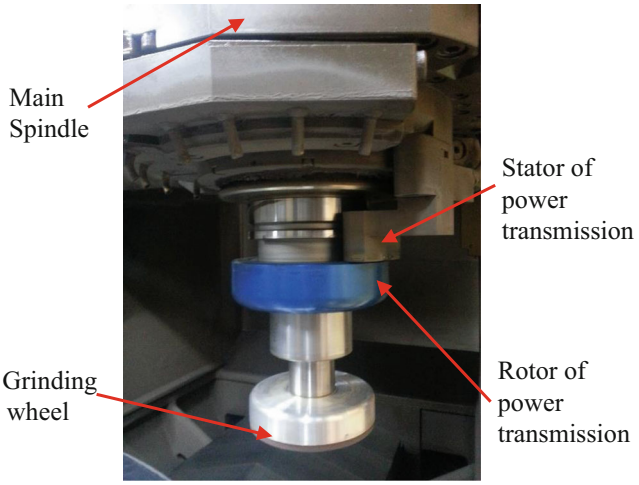

Fig. 6 Ultrasonic vibration system of the used machining center

3.2 Measurement of wheel wear amount

Evaluation of wheel edge profile was carried out using a CNC tool microset (DMG ECO 210) as shown in Fig. 10. After each grinding cycle, the tool holder with the grinding wheel was removed from the machining center spindle, and subsequently set onto the microset which has an air-bearing tool holder with high-precision taper bore. During measurement, a set of optical system was adopted to measure the edge profile of the grinding wheel. The movement along the *X*- and the *Y*-directions is supported by aerostatic guide ways with a 1-μm repositioning accuracy. Thus, the edge profile could be precisely measured.

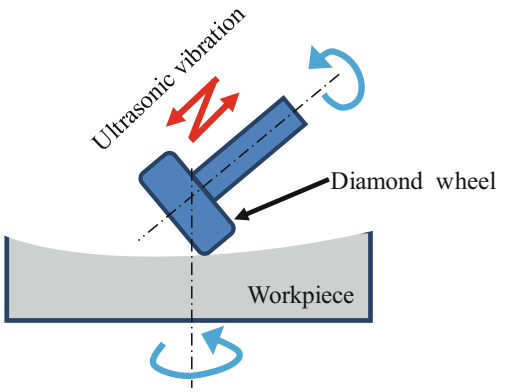

Fig. 7 The schematic of the inclined axis rotary ultrasonic grinding method

Table 1 Grinding conditions

Machining center	ULTRASONIC 210 P
Grinding wheel	Resin-bonded diamond wheel
Workpiece	Reaction-bonded SiC
Wheel rotation (rpm)	4000~6000
Table feed (mm/min)	80~1500
Depth of cut (mm)	0.05~0.5
Radial feed (mm/rpm)	0.1~2
Grinding fluid	Blaser Swisslube
Vibration frequency (kHz)	20~30

Measurement of wheel wear amount is based on the calculation of the wear volume that occurs on the wheel edge. Figure 11a shows the unused edge, and Fig. 11b shows a typical worn wheel from the CRT screen of the above-mentioned microset. Figure 12 schematically shows the calculation principle of the wear volume, which can be expressed as follows:

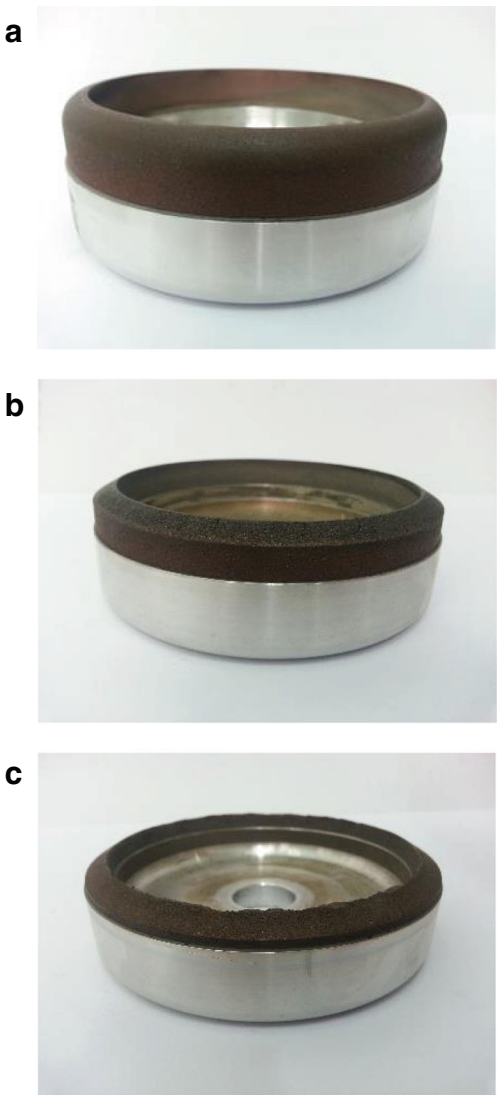

Fig. 8 Grinding wheel at different stages: **a** unused wheel, **b** after the first grinding cycle, and **c** after the second grinding cycle

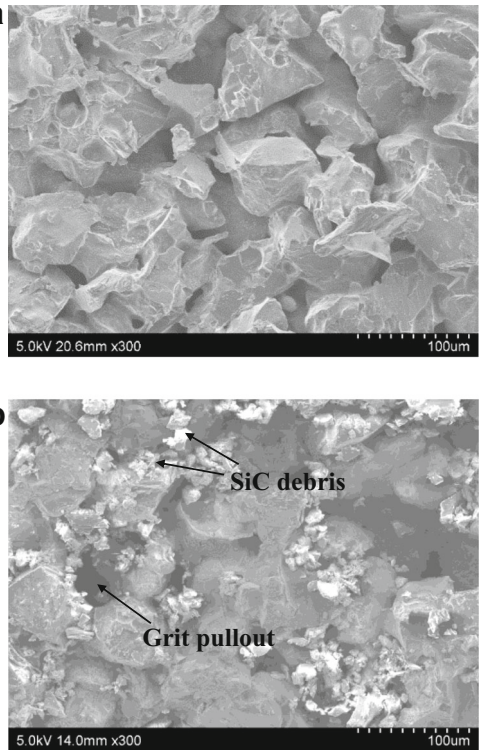

Fig. 9 SEM images showing the surface topography of the diamond wheel: **a** the unused wheel and **b** after the second grinding cycle

$$V_m = V_1 + V_2 - V_3 \tag{1}$$

where V_1 is the volume of $\overline{AB}$ rotating around the central axis, V_2 is the volume of arc $\overline{BC}$ rotating around the central axis, and V_3 is the volume of $f(x)$ rotating around the central axis.

Here, the V_1 can be expressed as follows:

$$V_1 = \int_a^b 2\pi x \times w\,dx \tag{2}$$

Fig. 10 Optical measurement of grinding wheel profile using a microset

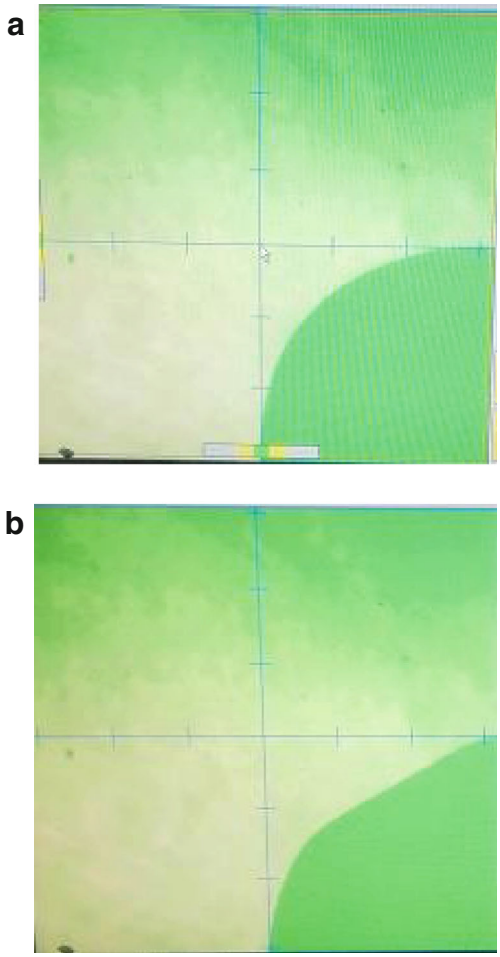

Fig. 11 The profile of the wheel edge: **a** unused wheel and **b** worn wheel

where w is the thickness of the abrasive layer. The V_2 can be expressed as follows:

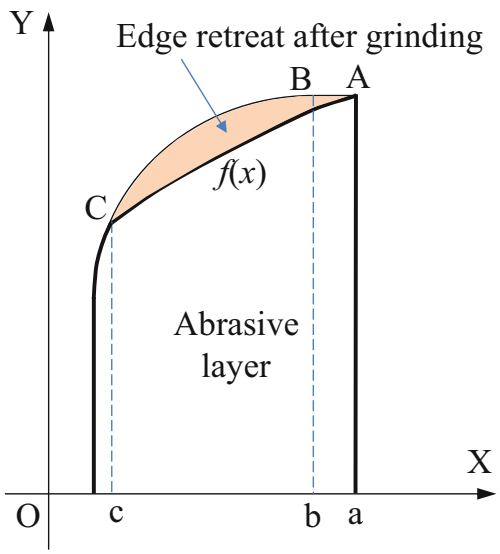

Fig. 12 Volume calculation of wheel wear amount

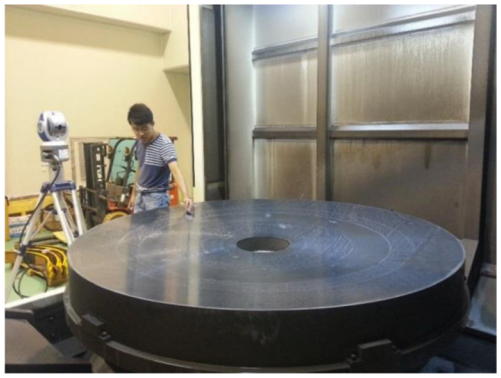

Fig. 13 Measurement of the surface form errror using a FARO laser tracker

$$V_2 = \int_a^b 2\pi x \times s\,(x)dx \tag{3}$$

where $s(x)$ is the wear area and can be expressed as follows:

$$s(x) = \sqrt{R^2-(x-b)} + (w-R) \tag{4}$$

where R is the radius of initial wheel edge. The profile of the worn edge can be measured and fitted as $f(x)$, then the V_3 can be expressed as follows:

$$V_3 = \int_a^c 2\pi x \times f\,(x)dx \tag{5}$$

3.3 Measurement of surface form error

There exists two ordinary methods for measuring surface form error, namely the coordinate measurement machine (CMM) and the infrared interferometer. Both methods are off-machine metrologies, having the risk in moving and relocating the large-scale workpiece. On the other hand, in order to rapidly measure the form error, a profilometer probe installed on the machine's spindle is always used. However, the obtained result includes the intrinsic motion error of the machine tool.

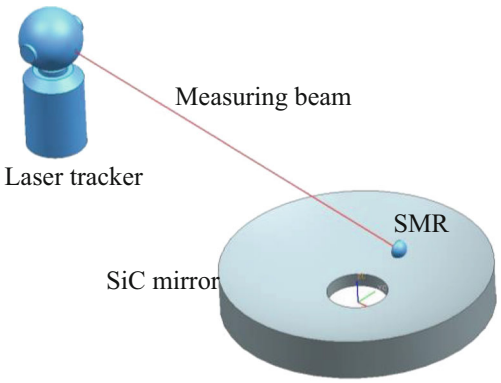

Fig. 14 Measurement principle of the laser track

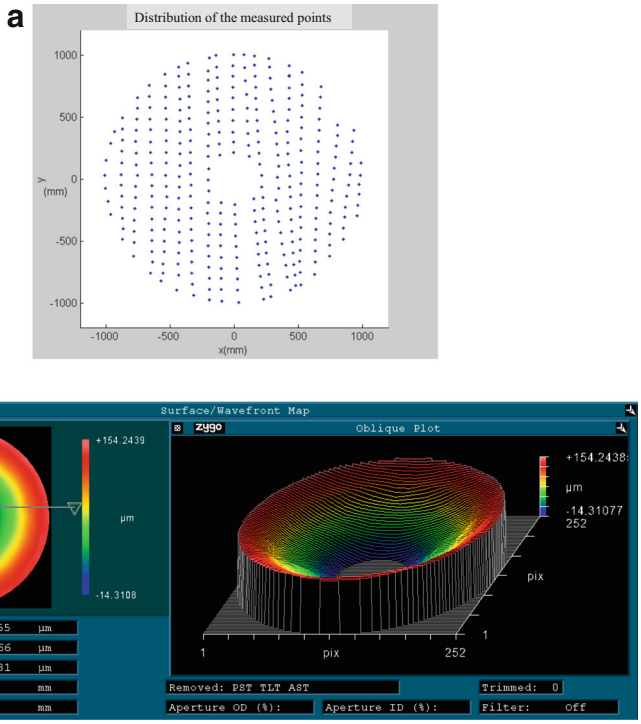

Fig. 15 Form error distribution of the ground surface: **a** a set of measured points and **b** the map of form error distribution

In this study, a FARO laser tracker as shown in Fig. 13 was used to measure the surface form error [20]. The laser tracker is capable of measuring a mirror surface to sub-micron accuracy. The surface measurement uncertainty is 0.6 µm. We have demonstrated this sort of accuracy in other measurement work. The basic principle of laser tracker measurement is shown in Fig. 14. The laser tracker combines a distance-measuring interferometer (DMI) with two angle encoders. Therefore, the laser tracker can measure a distance r and two angles α, β by tracking a laser beam to a spherically mounted retroreflector (SMR) held in contact with the ground surface to be measured. The coordinate of measured point could be obtained by the following equations:

$$\begin{cases} X = r\sin\beta\cos\alpha \\ Y = r\sin\beta\sin\alpha \\ Z = r\cos\beta \end{cases} \tag{6}$$

By the subtraction of the measured coordinates on ground surface from the theoretical ones import from a 3D geometry model, form error of the ground surfaces could be obtained.

Figure 15a, b shows a set of measured data points and the calculated form error distribution, respectively. In this measurement, a total of 345 data points were obtained in the measurement time of 25 min. The measurement time should not be too long so as to avoid the influence of environmental temperature changes on the measurement results. For the convenience of visualization of error distribution, the measurement data was processed using the Zygo software. It can be seen that the surface form error is very large, reaching 168 µm in PV and 96 µm in RMS. The form error distribution looks like a spherical aberration, in which the error gradually becomes larger and larger from the center to the edge of workpiece. That is due to the accumulation effect of wheel edge retreat when the wheel feeding from the center to the edge. Therefore, grinding wheel wear is the dominant factor of surface form error. Tool wear-induced surface form error should be emphatically compensated in grinding of the 2-m SiC workpiece.

3.4 In-process compensation of surface form error

Lots of research efforts have been reported toward at developing compensation technologies for wheel wear involved in grinding processes. As a common strategy, the ground surface was measured, and then, the measured result was used as a reference to modify the NC tool path for subsequent compensation grinding cycle [18, 21–24]. The common drawback is that the wheel wear in the compensation grinding which would introduce new form error has not been considered. In order to

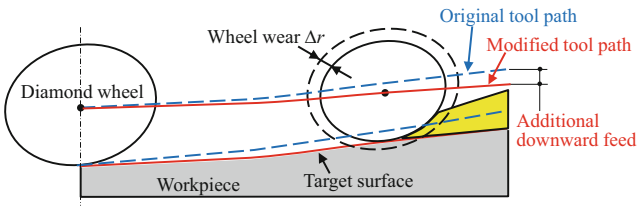

Fig. 16 Schematic of the in-process compensation method

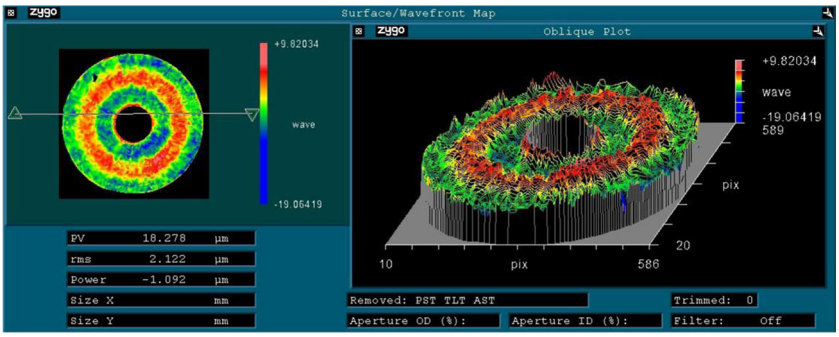

Fig. 17 Form error distribution of the ground surface after compensation grinding

achieve a satisfactory result, compensation grinding has to be repeated three to five grinding cycles. As a result, total grinding time turned to be very long because the grinding time of one grinding cycle for a 2-m scale workpiece is up to 15 h.

In order to shorten the time of compensation grinding, an in-process compensation strategy was developed in consideration of the wheel wear condition during compensation grinding process. As illustrated in Fig. 16, the wheel wear Δr was predicted in advance according to the wear volume of grinding wheel. Based on the predicted wheel wear Δr, the form error at certain point could be calculated. Subsequently, tool path of the wheel was modified by adding a downward feed to compensate the predicted wheel wear. There are two important issues that significantly affect the compensation accuracy and efficiency in this process. One is the way that the wheel wear amount is precisely predicted. The other is the method to modify the NC tool path in the grinding process.

By virtue of the in-process compensation method, surface form error of the 2-m SiC workpiece after one compensation grinding cycle was minimized to 18 μm in PV and 2 μm in RMS. This result is comparable to the grinding accuracy obtained by using the ultra-precision BoX® grinding machine in reference 14. Therefore, this work proved that even using a common-available machining center, similar surface form accuracy could be reached by means of the proposed grinding strategies. As shown in Fig. 17, the form error distribution looks like a set of concentric rings. The spherical error of the preliminary grinding surface in the previous section was dramatically reduced. In fact, the ring-like form error could be further reduced if compensation grinding was performed more times. However, because the ground surface will be further processed by subsequent lapping processes, the residual form error on ground surface was no longer compensated by the grinding process.

It is easy to understand that the larger the size of workpiece, the worse the surface form accuracy obtained. However, there is little quantitative description about the relationship between workpiece dimension and surface form accuracy. In this study, we presented a novel indicator, the accuracy-to-dimension ratio (ADR), to evaluate the grinding capability of SiC workpieces with different sizes. Table 2 shows the calculated ADR value of the small, the medium, and the large workpiece, respectively. It is surprising that although the sizes of the workpieces are different, the ADR values are all very close to 10^{-5}. Therefore, it is reasonable to say that we have achieved a high-precision SiC mirror blank by grinding even if its aperture diameter is up to 2 m.

3.5 Subsurface damages

Depth of subsurface damage layer is an important factor to determine convergence rate of surface form error in subsequent lapping process. In this study, subsurface damages of ground SiC samples were investigated by magnetorheological finishing (MRF) spot technique [25], which is less destructive and more efficient in measurement of subsurface damages compared with ball dimpling [26] and tapering methods [27]. Typical subsurface damages involved in the MRF spot are observed using the SEM. Figure 18a shows a ground surface where a large amount of microcraters in the order of 1~5 μm are clearly observed. Both the size and the number of the microcraters decrease gradually with the increase of depth as shown in Fig. 18b–d. In this study, it is not possible to obtain a crater-free surface by MRF polishing probably because of the inherent defects such as micropores in RB-SiC samples. It is also known from Fig. 18 that the microcraters are mainly distributed on the SiC grain surface. On the basis of the above findings, the depth of the subsurface damage layer is estimated as smaller than 5 μm. Therefore, production cycle time in the subsequent lapping and polishing processes of SiC will be dramatically reduced. As a contrast, no cracks were found on the subsurface damage layer, which

Table 2 The accuracy-to-dimension ratio (ADR) for SiC workpieces in different sizes

	Accuracy (PV)	Aperture	ADR
L. Yin [12]	0.13 μm	Φ 13.5 mm	0.0000096
X. Tonnellier [14]	5 μm	400 mm across corners	0.0000125
This study	18.27 μm	Φ 2000 mm	0.0000091

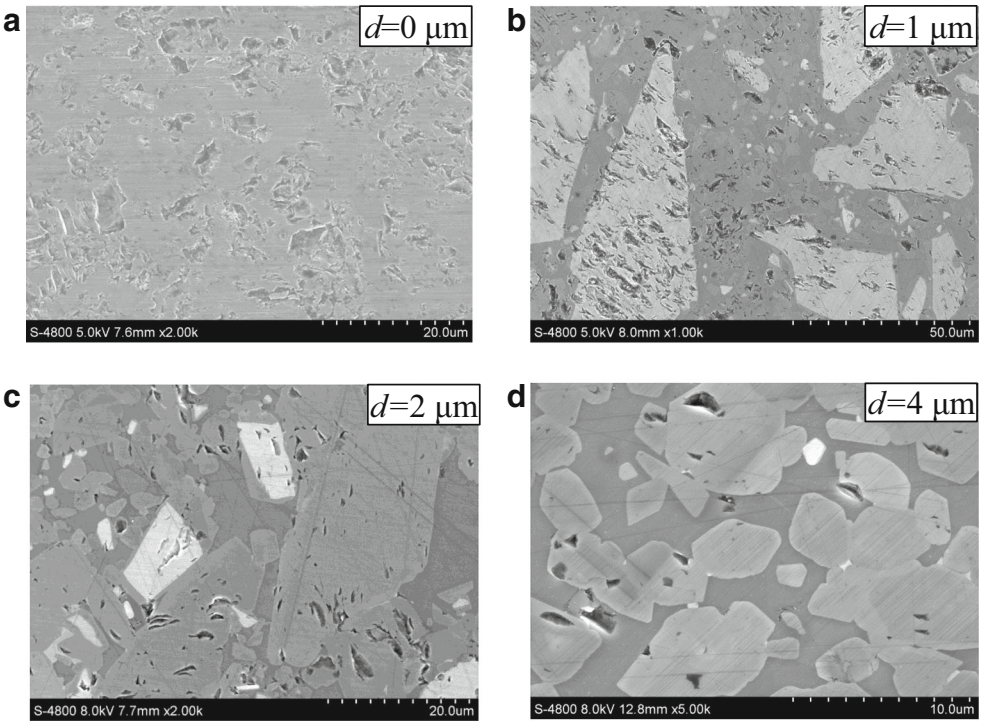

Fig. 18 Typical subsurface damages at different depth: **a** ground surface, **b** 1 μm, **c** 2 μm, **d** 4 μm

is dramatically different from the subsurface damages in grinding of the ULE and Zerodur glass.

In order to investigate the material removal behavior in grinding of RB-SiC, the ground surface was also analyzed using energy dispersive X-ray (EDX). Figure 19a shows the ground surface where both the smooth regions and the rough regions can be identified. Figure 19b–d provides the corresponding EDX map for O, C, and Si elements, respectively. It can be obviously distinguished that the smooth region corresponds to the enriched Si element and the absence of C

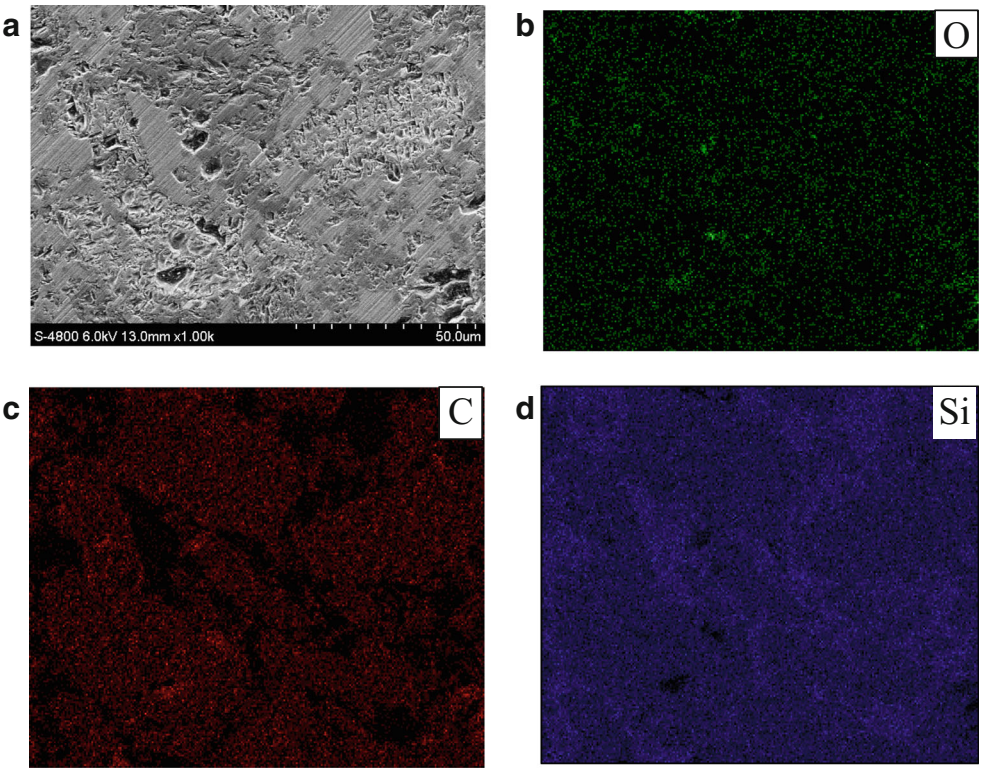

Fig. 19 SEM micrograph of ground surface (**a**) and EDX maps for O (**b**), C (**c**), and Si (**d**)

element. On the basis of the above results, it is believed that the residual Si bond material was removed by ductile grinding manner which introduces a relatively smooth region, while the SiC grain was removed by brittle manner which generates microcraters on the SiC grain surface.

4 Conclusions

A systematic research on the high-performance grinding of SiC workpiece has been presented to fabricate large-scale aspherical mirrors needed in high-resolution space-based telescopes. The following conclusions have been drawn:

(1) Wheel edge retreat is the dominant factor of surface form error in grinding of a 2-m SiC mirror blank. The form error of the ground surface is directly relied on the wheel wear amount other than the positioning accuracy of machining center.
(2) Measurement of surface form error by a laser tracker has been developed. Results showed that the laser tracker is an effective method to measure the large-scale ground surface.
(3) In-process compensation of surface form error was developed based on the wheel wear prediction and the modification of tool path.
(4) Due to the ultrasonic vibration, the self-dressing of grinding wheels occurs during the whole grinding cycle, which brings out an uninterrupted grinding of SiC mirror blank in a long time.
(5) Using the proposed grinding strategies, a 20-micron-order surface accuracy in PV, near the positioning accuracy of the used machining center, could be achieved.
(6) The accuracy-to-dimension ratio (ADR) was proposed to evaluate the grinding capability for SiC workpieces. It is shown that although the sizes of the workpieces are different, the ADR values obtained are all very close to 10^{-5}.
(7) Typical subsurface damage is the microcraters on SiC grain surface. Total depth of damage layer is estimated to be about 5 μm, far less than subsurface damage layer of the ULE and Zerodur.

Acknowledgments The authors would like to acknowledge funding supports from the National Natural Science Foundation of China (no. 51305422, no. 51505185). The authors also would like to thank Mr. He Huang and Jingwei Li for the grinding experiment support and Ms. Ling Xiong for technical support on surface form error measurement.

References

1. Lallo M (2012) Experience with the Hubble Space Telescope: 20 years of an archetype. Opt Eng 51(1):011011
2. Shore P, Cunningham C, Debra D, Evans C, Hough J, Gilmozzi R, Kunzmann H, Morantz P, Tonnellier X (2010) Precision engineering for astronomy and gravity science. CIRP Ann – Manuf Techn 59(2):694–716
3. Hull T, Westerhoff T (2014) Lightweight ZERODUR mirror blanks: recent advances supporting faster, cheaper, and better spaceborne optical telescope assemblies. Proc SPIE 9241
4. Tonnellier X, Morantz P, Shore P, Baldwin A, Evans R, Walker D (2007) Subsurface damage in precision ground ULE and Zerodur surfaces. Opt Express 15(19):12197–12205
5. Bougoin M, Deny P (2004) The SiC technology is ready for the next generation of extremely large telescopes. Proc SPIE 5494:9–18
6. Zhang XJ, Zhang ZY, Zheng LG (2005) Manufacturing and testing SiC aspherical mirrors in space telescopes. Proc SPIE 6024:1–5
7. Ealey M, Weaver G (1996) Developmental history and trends for reaction bonded silicon carbide mirrors. Proc SPIE 2587:66–72
8. Kitahara H, Noda Y, Yoshida F, Nakashima H, Shinohara N, Abe H (2001) Mechanical behavior of single crystalline and polycrystalline silicon carbides evaluated by Vickers indentation. J Ceram Soc Jpn 109:602–606
9. Wilson R (2002) Reflecting telescope optics II: manufacture, testing, alignment, Modern Techniques. Springer-Verlag, New York, LLC
10. Cheng H, Feng Z, Lei S, Wang Y (2005) Magnetorheological finishing of SiC aspheric mirrors. Mater Manuf Process 20(6): 917–931
11. Weiser M (2009) Ion beam figuring for lithography optics. Nucl Instr Meth Phys Res B 269(8–9):1390–1393
12. Yin L, Vancoille E, Lee L, Huang H, Ramesh K, Liu X (2004) High-quality grinding of polycrystalline silicon carbide spherical surfaces. Wear 256:197–207
13. Comley P, Morantz P, Shore P, Tonnellier X (2011) Grinding metre scale mirror segments for the E-ELT ground based telescope. CIRP Ann – Manuf Techn 60:379–382
14. Tonnellier X (2009) Precision grinding for rapid manufacturing of large optics. Cranfield University, England
15. Zhang T, Zhang ZQ, Zhang JX, Jiang DL, Lin QL (2007) Preparation of SiC ceramics by aqueous gelcasting and pressureless sintering. Mater Sci Eng A 443(1–2):257–261
16. Suyama S, Kameda T, Itoh Y (2003) Development of high-strength reaction-sintered silicon carbide. Diamond Relat Mater 121201: 1204
17. Kuriyagawa T, Zahmaty M, Syoji K (1996) A new grinding method for aspheric ceramic mirrors. J Mater Process Technol 62(4):387–392
18. Chen FJ, Yin SH, Ohmori H, Yu J (2012) Form error compensation in single-point inclined axis nanogrinding for small aspheric insert. Int J Adv Manuf Tech 65(1–4):433–441
19. Zhang ZY, Zheng LG (2013) Grinding strategies for machining the off-axis aspherical reaction-bonded SiC mirror blank. Chin Opt Lett 12(1):S12202–S12206
20. Su P, Oh C, Zhao CY, Burge J (2012) Optical testing for meter size aspheric optics. Proc SPIE 8466:84660S
21. Chen FJ, Yin SH, Huang H, Ohmori H, Wang Y, Fan YF, Zhu YJ (2010) Profile error compensation in ultra-precision grinding of

aspheric surfaces with on-machine measurement. Int J Adv Manuf Tech 50:480–486
22. Li DD, Xu MM, Wei CJ, Hu DJ, Xu LM (2011) Error analysis and in-process compensation on cup wheel grinding of hard sphere. Int J Adv Manuf Tech 515:43–548
23. Rahman M, Saleh T, Lim H, Son S, Rahman M (2008) Development of an on-machine profile measurement system in ELID grinding for machining aspheric surface with software compensation. Int J Adv Manuf Tech 48:887–895
24. Nakai M, Aguiar P, Jr H, Bianchi E, Spatti D, Addona D (2015) Evaluation of neural models applied to the estimation of tool wear in the grinding of advanced ceramics. Expert Syst Appl 42:7026–7035
25. Li SY, Wang Z, Wu YL (2008) Relationship between subsurface damage and surface roughness of optical materials in grinding and lapping processes. J Mater Process Technol 205:34–41
26. Lambropoulos JC (1998) Micromechanics of material-removal mechanisms from brittle surfaces. LLE Review 74:131–138
27. Esmaeilzare A, Rahimi A, Rezaei SM (2014) Investigation of subsurface damages and surface roughness in grinding process of Zerodur glass-ceramic. Appl Surf Sci 313:67–75